Solar cycle–dependent helicity transport by magnetic clouds

B. J. Lynch,[1] J. R. Gruesbeck, and T. H. Zurbuchen
Department of Atmospheric, Oceanic, and Space Sciences, University of Michigan, Ann Arbor, Michigan, USA

S. K. Antiochos[2]
E. O. Hulburt Center for Space Research, Naval Research Laboratory, Washington, D.C., USA

Received 14 March 2005; revised 3 May 2005; accepted 20 May 2005; published 25 August 2005.

[1] Magnetic clouds observed with the Wind and ACE spacecraft are fit with the static, linear force-free cylinder model to obtain estimates of the chirality, fluxes, and magnetic helicity of each event. The fastest magnetic clouds (MCs) are shown to carry the most flux and helicity. We calculate the net cumulative helicity which measures the difference in right- and left-handed helicity contained in MCs over time. The net cumulative helicity does not average to zero; rather, a strong left-handed helicity bias develops over the solar cycle, dominated by the largest events of cycle 23: Bastille Day 2000 and 28 October 2003. The majority of MCs ("slow" events, $\langle V_r \rangle < 500$ km/s) have a net cumulative helicity profile that appears to be modulated by the solar activity cycle. This is far less evident for "fast" MC events ($\langle V_r \rangle \geq 500$ km/s), which were disproportionately left-handed over our data set. A brief discussion about the various solar sources of CME helicity and their implication for dynamo processes is included.

Citation: Lynch, B. J., J. R. Gruesbeck, T. H. Zurbuchen, and S. K. Antiochos (2005), Solar cycle–dependent helicity transport by magnetic clouds, *J. Geophys. Res.*, *110*, A08107, doi:10.1029/2005JA011137.

1. Introduction

[2] Coronal mass ejections (CMEs) are violent eruptions of magnetic field and plasma from the low solar corona into interplanetary space. The most magnetically structured CMEs are observed in situ by spacecraft as strong, coherent field rotations with low proton temperature. This subset of interplanetary CMEs (ICMEs) are now referred to as magnetic clouds (MCs) [*Burlaga*, 1991, and references therein].

[3] The configuration of the magnetic structure of these ejecta has been an important contribution to the investigation of eruptive solar features, their source environment, and the corresponding observed plasma in the heliosphere. A key element of these investigations have been the chirality or handedness (sense of twist) of the magnetic field, i.e., the sign of the magnetic helicity.

[4] Magnetic helicity is a topological quantity that measures the linkage of flux systems and is approximately conserved during magnetic reconnection [*Matthaeus and Goldstein*, 1982; *Brown et al.*, 1999]. (Throughout the paper, we will commonly use the term helicity with the understanding that we are always referring to magnetic helicity.) Therefore it has become one of the primary tools in the association of various solar magnetic sources with in situ interplanetary field measurements.

[5] Many solar phenomena have been observed to have similar, and thus probably fundamentally related, dependence on magnetic helicity. There is a persistent trend that associates the chirality of the the Northern Hemisphere with left-handed (negative) helicity and the Southern Hemisphere with right-handed (positive) helicity, independent of solar cycle. This trend has been observed in active region photospheric and coronal fields [*Pevtsov et al.*, 1995; *Canfield and Pevtsov*, 1999], sunspot whorls [*Richardson*, 1941; *Ding et al.*, 1987], and filaments, filament channels, and their overlying fields [*Martin et al.*, 1994; *Martin and McAllister*, 1996].

[6] The hemispheric chirality trend also extends into interplanetary space, i.e., Northern Hemisphere eruptions tend to evolve into left-handed magnetic clouds and Southern Hemisphere eruptions into right-handed magnetic clouds [e.g., *Rust*, 1997; *Marubashi*, 1997; *Yurchyshyn et al.*, 2001]. *Rees and Forsyth* [2003] showed that the sign of the magnetic cloud axial field observed in high-latitude events is in good agreement with the *Bothmer and Schwenn* [1998] "prediction" that the axial field might follow the Hale polarity for sunspot pairs in their respective hemispheres. Assuming the leading and trailing fields in these high-latitude MCs are driven by the the global solar dipole [*Bothmer and Rust*, 1997], then these observations also support the Northern/Southern Hemisphere LH/RH chirality trend. However, this chirality dependence is only an average trend and not necessarily true on a case by

[1] Also at the E. O. Hulburt Center for Space Research, Naval Research Laboratory, Washington, D.C., USA.
[2] Also at the Department of Atmospheric, Oceanic, and Space Sciences, University of Michigan, Ann Arbor, Michigan, USA.

0148-0227/05/2005JA011137

case basis, for example, the distribution of S (RH) and inverse-S (LH) sigmoids in their "expected" hemispheres is ~60–70% [*Pevtsov and Canfield*, 1999; *Pevtsov et al.*, 2001].

[7] *Leamon et al.* [2002, 2004] found that for individual events, the direct correspondence between the chirality of an erupting active region and the handedness of the subsequent magnetic cloud seems least likely to apply during solar maximum, leading those authors to conclude that the in situ fields are a combination of both active region and overlying background field.

[8] A number of authors argue that CMEs may play a key role in the long-term evolution of the global solar magnetic field [e.g., *Rust*, 1994, 1997, 2001; *Bieber and Rust*, 1995; *Low*, 1996, 1997, 2001; *Zhang and Low*, 2001]. They state that CMEs are the primary mechanism of removing the flux and/or helicity associated with the previous cycle's polarity, enabling the new cycle's field of opposite polarity to emerge without an infinite accumulation of flux or helicity in the solar corona. There seems to be some tentative observational and theoretical support. *Gopalswamy et al.* [2003a] show that the solar pole reversals coincide with the sudden cessation of high-latitude CMEs and erupting prominences. *DeVore* [2000] used numerical simulations to show that the helicity generated by surface differential rotation of bipolar active regions is consistent with the helicity removed by CMEs idealized as magnetic clouds over an entire solar cycle. However, other researchers, when looking at specific active regions and their CMEs, conclude more helicity is transported by the CMEs (as ideal MCs) than is generated by the observed shearing motions during the active region lifetime [*Démoulin et al.*, 2002; *Green et al.*, 2002; *Nindos and Zhang*, 2002; *Nindos et al.*, 2003]. This implies a more direct dynamo coupling to the source of CME helicity at least for some active regions. *Berger and Ruzmaikin* [2000] have studied the solar dynamo production of helicity via the Ω-effect (interior differential rotation) and shown that it produces helicity with the correct hemispheric trend and in sufficient quantities to easily account for the observational estimates of CME helicity transport over the solar cycle.

[9] The solar wind carries the interplanetary magnetic field (IMF) and its helicity into the heliosphere. The *Parker* [1963] field configuration contains helicity at the largest spatial scales of many AUs [*Bieber et al.*, 1987a] and the magnetic fluctuations of IMF turbulence contain helicity through spatial scales of ~0.01 AU or smaller [*Smith*, 1999, and references therein]. In fact, magnetic clouds are IMF features corresponding to spatial scales of ~0.1–0.3 AU, i.e., coherent field structures lasting on the order of tens of hours in duration [*Burlaga*, 1991]. *Smith* [1999] showed that the helicity correlation function from the IMF turbulence has the dominant peak in the 10–20 hour time lag range, suggesting that magnetic clouds are one of the most important contributors to the helicity convected into the heliosphere.

[10] It may not be surprising that the helicity carried by IMF turbulence exhibits solar cycle variation. This is a crucial ingredient for understanding the large-scale topology of the heliosphere and the particles propagating within it. For example, *Bieber et al.* [1987b] have shown that the solar cycle variation of IMF helicity density of "toward" and "away" (positive and negative) magnetic sectors have direct consequences for galactic cosmic rays. In these studies, *Bieber et al.* [1987b] and *Smith* [1999] have shown there is a persistent hemispheric asymmetry in the IMF turbulence net helicity density and that it also shows solar cycle modulation over the past 30 years.

[11] In this paper, we study the large-scale, long-term ordering of helicity in magnetic clouds during solar cycle 23. We show that there is a definite link between the solar activity cycle and the helicity content of magnetic clouds. *Lynch et al.* [2003, hereinafter referred to as LY03] presented initial findings that suggested the fastest cloud events (which occur during solar maximum and the declining phase) carry the most helicity. The results herein will show for solar cycle 23 the net helicity carried by magnetic clouds is right-handed during solar minimum (1995–1996) and proceeds to change sign over the activity cycle, resulting in a strong left-handed helicity preference by the end of our data set (2003). An immediate comparison to the *Bieber et al.* [1987b] and *Smith* [1999] results is complicated by the fact that we start our net helicity (arbitrarily) at zero and do not order our in situ observations by the polarity of the background field (i.e., the MC occurrence in "toward" or "away" magnetic sectors).

[12] The organization of the paper is as follows. Section 2 describes the magnetic cloud survey, where we have updated the LY03 model fitting and expanded the event list. Section 3 discusses magnetic cloud speeds in relation to the solar cycle, confirming solar cycle trends reported in more general LASCO and in situ CME/ICME surveys. We then show a significant correlation between the event average radial velocity $\langle V_r \rangle$, the derived cloud radius R_c, and model axial field strength. In section 4 we show the net cumulative helicity transported by magnetic clouds develops a strong left-handed preference during the cycle 23 solar maximum, affected largely by the fastest events of the survey. When the fast magnetic cloud events ($\langle V_r \rangle \geq$ 500 km/s) are excluded, the net helicity shows relatively smooth, sinusoidal variation that appears to track the solar activity cycle. Section 5 concludes with a brief discussion about the different sources of helicity shed by eruptions during the solar cycle.

2. Magnetic Cloud Observations

2.1. Magnetic Cloud Description and Survey Details

[13] Magnetic clouds are the most structured subset of ICMEs observed in the heliosphere. The *Burlaga* [1988] identification criteria are (1) enhanced magnetic field magnitude, (2) a smooth rotation of the magnetic field direction over a large angle, and (3) low proton-temperature (or a low plasma β_p, the ratio of proton gas pressure to magnetic pressure). However, the requirements as stated are not quantitative, so there is room for interpretation. For example, *Cane and Richardson* [2003] identify a large subset of ICMEs that show some coherent field organization but are not easily fit with a simple force-free magnetic field model. *Zhang et al.* [2004] called these cloud-like ICMEs "quasi-clouds." For additional discussion of the borderline qualifications (e.g., no significant field strength enhancement, smooth rotation over a small angle) and boundary selection ambiguities, see section 2 of LY03.

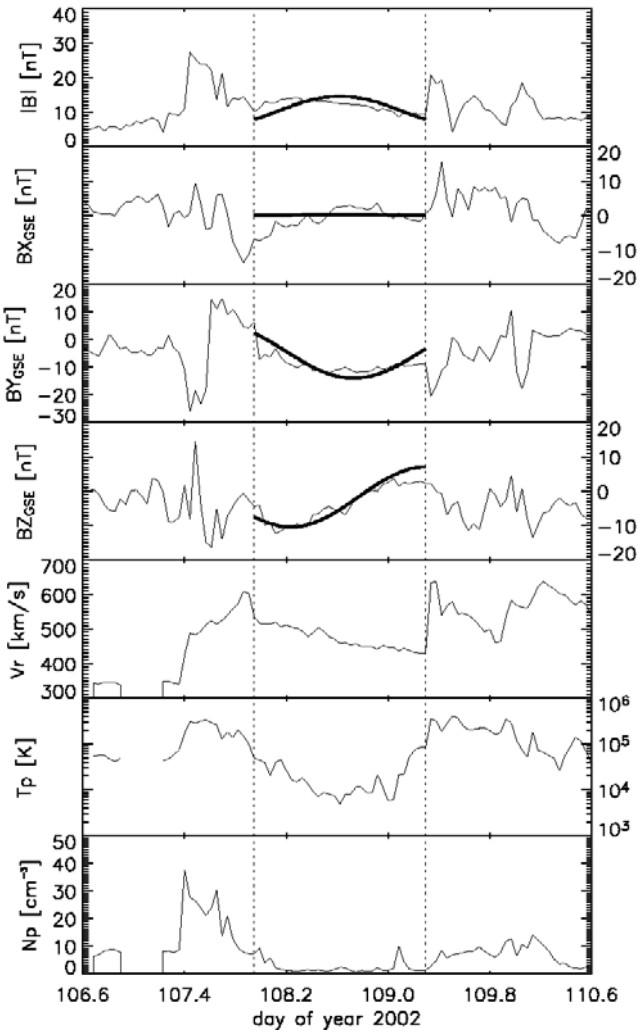

Figure 1. The magnetic cloud event of 17 April 2002 observed by the ACE spacecraft. The data shown from top to bottom are hourly averages of the magnetic field magnitude, field components in GSE coordinates, the radial velocity, proton temperature, and proton density. The vertical dotted lines indicate the cloud region and the thick solid black lines are the linear force-free model fit with parameters $\phi_0 = 271°$, $\theta_0 = -21.3°$, $\rho_0 = 0$, $H = +1$, and $B_0 = 14.6$ nT.

[14] We have improved the event selection procedure of LY03 by applying a more quantitative treatment of the low proton temperature requirement. Following *Richardson and Cane* [1995], we compare the proton temperature to their empirical expected proton temperature T_{ex}. If $\langle T_p \rangle \leq 0.5 \langle T_{ex} \rangle$ (the averages are over the event interval), the event immediately met the low proton temperature requirement. If $0.5 \langle T_{ex} \rangle < \langle T_p \rangle \leq \langle T_{ex} \rangle$, we looked at the event averaged value of $\beta_p = n_p k T_p / (B^2/2\mu_0)$. Events with $\langle \beta_p \rangle \leq$ O(0.1) were also included.

[15] Using published and public ICME and magnetic cloud lists from LY03, *Cane and Richardson* [2003], *Zhang et al.* [2004], and the Wind spacecraft (http://lepmfi.gsfc.nasa.gov/mfi/mag_cloud_pub1.html) as guides, we have compiled an event list of 132 magnetic clouds from 1995 through 2003 and fit each event with the cylindrically symmetric, linear force-free model. The total event list and the model fit parameters described in the following section can be found as auxiliary material to this paper.[1]

2.2. Linear Force-Free Model and Parameter Fitting

[16] The structured internal fields are modeled with the standard *Burlaga* [1988] approach and fit via a two-step least squares procedure, similar to *Lepping et al.* [1990]. However, our model differs from the standard *Lepping et al.* [1990] implementation in that we assume the closest point of approach is necessarily at the temporal midpoint of the cloud event and the cloud radius R_c is not an additional free parameter but determined strictly from the geometry of a static cylinder.

[17] The magnetic cloud model is the linear force-free, constant-α solution of the equation $\nabla \times \mathbf{B} = \alpha \mathbf{B}$ in cylindrical coordinates. This is given by the *Lundquist* [1950] Bessel function solution,

$$\mathbf{B} = HB_0 J_1(\alpha\rho)\hat{\phi} + B_0 J_0(\alpha\rho)\hat{z}. \quad (1)$$

In our implementation of this model, there are five parameters. The three-dimensional (3-D) orientation of the cylinder in space is described the two angles ϕ_0, θ_0 of the symmetry axis and the impact parameter ρ_0 indicating the minimum distance between the spacecraft and the cylinder axis. B_0 is the magnetic field strength on the cylinder axis and H is the model handedness or chirality of the flux-rope. Right-handed and left-handed rotations have $H = +1$ and $H = -1$, respectively.

[18] Figure 1 shows a magnetic cloud observed by the ACE spacecraft on 17 April 2002. The magnetic field magnitude and field components in GSE coordinates are shown, along with the radial velocity, proton temperature, and density. The vertical dotted lines indicate the cloud region and the thick solid lines are the best-fit linear force-free cylinder model to the field rotations. The cloud region shows the characteristic linear decrease in radial velocity, indicating cloud expansion, and depressed proton temperatures.

[19] Our implementation of the linear force-free cylinder model has been rewritten since LY03 to allow for greater ease of comparisons with other authors' versions of similar models. The first minor change was conversion to a GSE coordinate system. The fit parameter angles are now defined in the GSE sense, i.e., positive ϕ_0 goes from $+\hat{x}$ (pointing toward the Sun) to $+\hat{y}$ (pointing east when looking from the Earth). Our parameter H has been redefined so that it represents the flux-rope handedness independent of coordinate system. This eliminates the need for equation (5) of LY03. Also, ρ_0 is allowed to vary between $(-1, 1)$ as it represents the normalized y-axis intercept in the cloud frame.

[20] The best fit parameters are obtained by minimizing error norms associated with the direction and magnetic field magnitude separately, comparable to *Lepping et al.* [1990]. The details of this procedure are described in section 3.2 of LY03, and we shall avoid repeating them here.

[1] Auxiliary material is available at ftp://ftp.agu.org/apend/ja/2005JA011137.

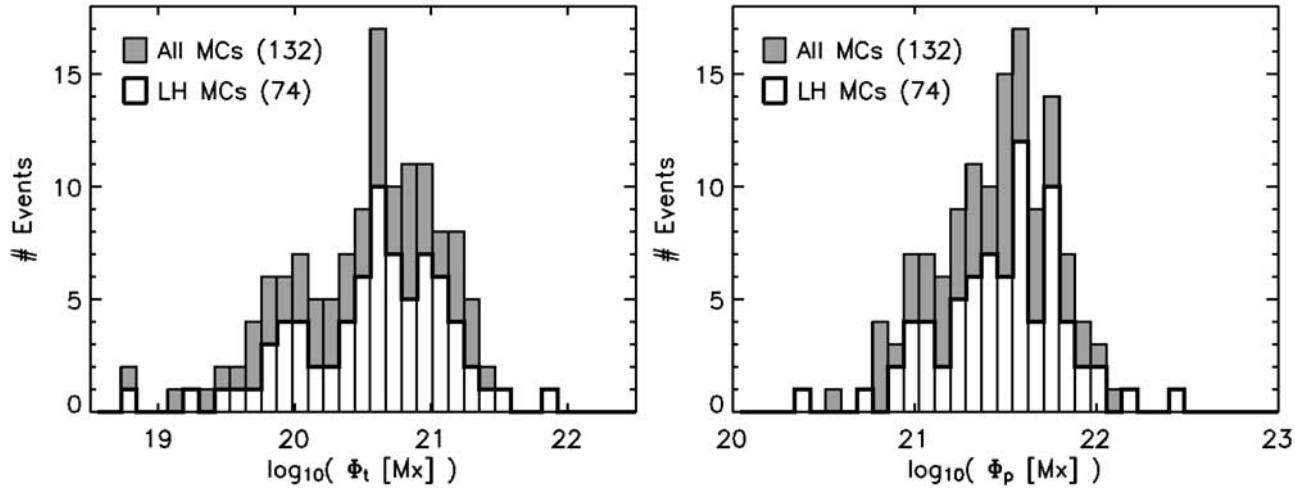

Figure 2. Histograms of logarithmic toroidal (left) and poloidal (right) flux for magnetic clouds (approximated by the LFF cylinder model). The histograms for all cloud events are shown in gray and the left-handed clouds are in white.

[21] There are limitations of this fitting procedure that have to be recognized. In particular, in LY03, we have shown that the fit parameters are often highly correlated, and consequently the minimum error fits are not always independent. *Lepping et al.* [2003] have presented a thorough investigation of the uncertainties in the fit parameters by adding various levels of simulated trend noise to known solutions. In Appendix A, we list our estimates of the fit parameter uncertainties obtained from the error minimization routine, which are in good agreement with the *Lepping et al.* [2003] results. *Leamon et al.* [2004] have examined several authors fits to the Bastille Day 2000 event and noted quite a range of best-fit values, although they are all pretty consistent given the large systematic model uncertainties. Also, recently, *Riley et al.* [2004] have examined the results of a number of different magnetic cloud model fits to their MHD simulation of a flux-rope CME. They found good agreement between various groups and their models for synthetic spacecraft data that cut through the center of the ejecta, but for high-impact, glancing trajectories (e.g., $|\rho_0| \geq \sim 0.7$), the disagreement between the model fit orientations could be even larger than reasonable estimates of the systematic uncertainties. In these high-impact cases the best-fit results can also become very sensitive to the selected event boundaries.

[22] However, despite the limitations of these simple models, due largely to the fact that we are inferring an often very idealized 3-D heliospheric structure from a one-dimensional spacecraft measurement, there has been valuable physical insight gained from employing these flux-rope model fits to magnetic cloud observations, as discussed in section 1. Also, the two most robust quantities derived from these fits are the chirality of the field rotations and the estimate of the axial field strength [*Lepping et al.*, 2003]. In the following analysis, we show that the long-term physical trends that emerge from the data are readily distinguished from the uncertainty inherent in any single model fit. We also note that any systematic model errors (like the cylindrical symmetry assumption) are common throughout the data set and therefore the results should remain qualitatively intact through any consistent model correction or improvement.

2.3. Model Flux and Helicity

[23] The toroidal flux of the magnetic cloud model is the axial field (the z-component of **B** in equation (1)) passing through the cylindrical cross section, whereas the poloidal field corresponds to the azimuthal field ($\hat{\phi}$ direction) integrated over an area the length of the flux-rope and from the axis to the cylinder radius. If both ends of the magnetic cloud flux-rope are assumed to be connected to the Sun, then only the poloidal field is removed from the corona by the eruption. However, observations show that magnetic cloud events are not always firmly connected at both footpoints of the flux-rope [*Shodhan et al.*, 2000] and some models for the gradual erosion of closed CME field lines have been presented [*McComas et al.*, 1995; *Crooker et al.*, 2002; *Reinard and Fisk*, 2004].

[24] The magnetic cloud toroidal flux is easily calculated from equation (1) and the cylindrical geometry,

$$\Phi_t = \int \mathbf{B} \cdot \hat{z}\, da = \frac{2\pi J_1(x_{01})}{x_{01}} B_0 R_c^2. \tag{2}$$

Here, x_{01} is the first zero of J_0 ($\sim$2.405) with α, the force-free parameter, defined such that $\alpha R_c = x_{01}$. The model poloidal flux is calculated in a similar fashion,

$$\Phi_p = \int \mathbf{B} \cdot \hat{\phi}\, da = \frac{L}{x_{01}} B_0 R_c, \tag{3}$$

where it the cylinder has an axial length L which grows with the flux-rope propagation. Since we are interested in the fluxes and magnetic helicity at Earth, we need an estimate of the magnetic cloud length at 1 AU. We use the *Leamon et al.* [2004] approximation of $L = 2.5$ AU, which is based on a direct observation of L by *Larson et al.* [1997] and simple geometrical reasoning.

[25] Figure 2 shows the distribution of both toroidal and poloidal fluxes for our entire data set. The thick solid lines

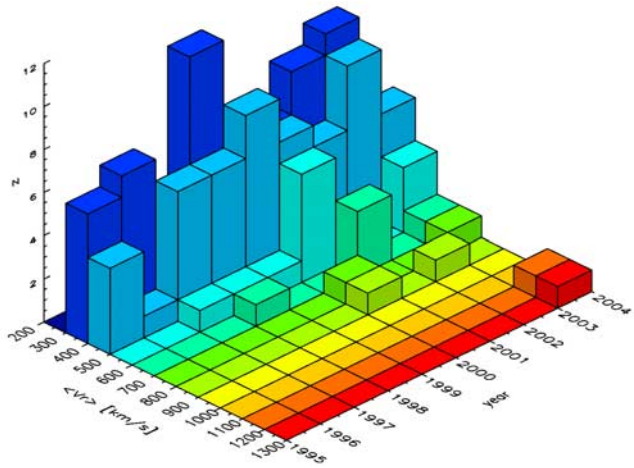

Figure 3. The two-dimensional histogram of MC average radial velocity for each year. The color scale is to ease the comparison of the different speed bins.

(gray bars) indicate the left-handed (right-handed) distribution. The flux carried by magnetic clouds seem to be pretty consistently between 10^{19}–10^{22} Mx with averages, $\langle\Phi_t\rangle$ = 6.62 × 10^{20} Mx and $\langle\Phi_p\rangle$ = 3.80 × 10^{21} Mx.

[26] The magnetic helicity of our linear, force-free model is defined as $K = \int_V \mathbf{A} \cdot \mathbf{B}\, dV$ where the magnetic vector potential $\mathbf{A}$ satisfies $\nabla \times \mathbf{A} = \mathbf{B}$ and the volume is that of the idealized cylinder ($\pi R_c^2 L$). The helicity carried by these *Lundquist* [1950] solution flux-ropes has been shown to be proportional to Φ_t^2 [e.g., *Bieber and Rust*, 1995; *Dasso et al.*, 2003]. From equations (1) and (2), one obtains,

$$K = \frac{1}{\alpha}\int_V B^2\, dV = \frac{\alpha L}{2\pi}\Phi_t^2 = \frac{x_{01}}{2\pi} L B_0^2 R_c^3. \tag{4}$$

Recent analysis by *Dasso et al.* [2003] have shown that the derived flux and helicity are almost independent (∼10% variation) of the exact field model used (e.g., Lunquist versus Gold-Hoyle), provided the spacecraft data are well fit. However, this seems to be consistently smaller than the inherent systematic uncertainties in the fit parameter values for any kind of model [*Lepping et al.*, 2003], or the variation between different user's fits for similar models, both having ∼20–30% variation [*Leamon et al.*, 2004; *Riley et al.*, 2004].

3. MC Velocities Over the Solar Cycle

3.1. Fast Events During Solar Max and the Declining Phase

[27] The magnetic cloud average radial velocity distribution and its evolution from solar minimum to maximum is shown in Figure 3. The 2-D histogram shows the velocity distribution of the MCs observed that year. The color scale shows the radial velocity. As the solar cycle increases, there is not only an increase in the number of fast events, but in their proportion of the number of total events during solar maximum and the declining phase.

[28] This trend has been seen in several other long-term CME studies. For example, *Gopalswamy et al.* [2003b] looked at CMEs measured by the Large Angle Spectrometric Coronagraph (LASCO) instruments [*Brueckner et al.*, 1995] aboard the SOHO spacecraft and showed that the mean CME speed is ∼1.8 times higher in 2002, just after solar maximum, than in solar minimum, 1996. *Cane and Richardson* [2003] discussed an extensive list of ICMEs identified by a number of field and plasma signatures. For the subset of ICME events identifiable with LASCO events, the ICME transit time shows a clear solar cycle dependence, with a vast majority of the fastest events occurring during the years of solar maximum 2000–2002.

[29] It has been established that the fastest solar eruptions originate from active regions [e.g., *MacQueen and Fisher*, 1983; *Sheeley et al.*, 1985; *Andrews*, 2002], and thus have occurrence rates that are solar cycle–dependent. LY03 noticed that the fastest magnetic clouds tended to have the largest toroidal fluxes. To investigate this further, we looked for possible correlations between several model fit parameters characterizing the magnetic cloud and the observed average radial velocity.

3.2. MC Parameter Correlations With $\langle V_r \rangle$

[30] Figure 4 shows the two magnetic cloud quantities used to derive the fluxes and helicity of the simple linear force-free cylinder model, plotted against their event averaged radial speed. The top panel is the magnetic cloud cylinder radius R_c, and the bottom panel is the model axial field strength B_0. In both plots the right-handed events are plotted with a diamond and the left-handed events are plotted with an asterisk. The estimated error bars, δR_c, δB_0, and $\delta\langle V_r\rangle$ are given in Appendix A.

[31] In order to quantify these correlations, we employ the nonparametric (rank-ordered) correlation test of the weighted t-statistic, t_w [*Porter and Klimchuk*, 1995, and references therein]. The distribution of t_w for uncorrelated data is well approximated by a zero-mean Gaussian with unit variance. Therefore testing the null hypothesis of uncorrelated data only requires a relatively simple calculation of the probability (and significance) of obtaining a value of $\geq|t_w|$, e.g., a $|t_w|$ = 2.0 would imply ∼2.3% chance of no correlation (the probability of a $\geq 2\sigma$ event). Utilizing this measure, we can effectively rule out that the data are uncorrelated, but we do not characterize the mathematical form of the correlation.

[32] For the (R_c, $\langle V_r\rangle$) data we use δR_c^{-1} as weights obtaining $|t_w|$ = 2.96 and a probability of being uncorrelated of 0.30%. This result may at first seem trivial because R_c is a function of the event averaged velocity $\langle V_r\rangle$ (see equation (A4)). However, the R_c functional dependence is on the product $\Delta T\langle V_r\rangle$, where ΔT is the observed cloud duration. This product is independent of $\langle V_r\rangle$ because given a cylinder of fixed radius, if one doubles its speed, the observed duration would be halved. Thus the observed (R_c, $\langle V_r\rangle$) correlation represents an actual physical relationship in the data. Assuming the event duration is related to the initial size and the ejecta expansion history, it seems reasonable that from an energy point of view, events launched faster, expand faster. The expansion would be largely driven by magnetic pressure close to the Sun and by the kinematic effects of spherical expansion further out [*Riley and Crooker*, 2004].

[33] The (B_0, $\langle V_r\rangle$) data show a similar velocity correlation. Using the $\delta\langle V_r\rangle^{-1}$ weighting gives a $|t_w|$ = 3.33 and a

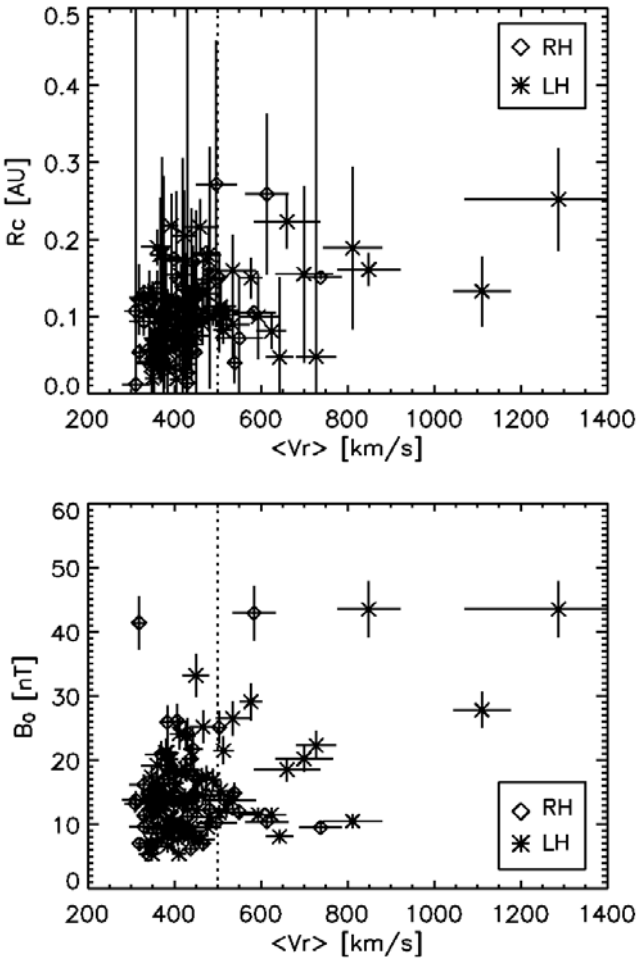

Figure 4. The two-dimensional distributions of magnetic cloud fit and data parameters and their associated uncertainties. The top and bottom panels show derived cloud size and model axial field strength, both plotted against average radial velocity. Both model quantities are correlated (with a high degree of confidence, see text) with the event averaged radial velocity. The vertical dotted line indicates the LY03 division between fast and slow MC events.

probability of being uncorrelated of 0.09%. A relationship between CME speed and source region field strength may be expected if CME dynamics in the low corona occur at characteristic speeds of order the Alfven speed, as would be the case in processes driven by magnetic reconnection. If we take typical quiet Sun (QS) and active region (AR) field strengths and densities as $B_{QS} \sim 1$ G, $n_{QS} \sim 5 \times 10^7$ cm^{-3} and $B_{AR} \sim 50$ G, $n_{AR} \sim 10^9$ cm^{-3}, then we get the ratio of Alfven speeds $(V_A)_{AR}/(V_A)_{QS} \sim 10$. This trend has also been seen in numerical simulations of the breakout model for CME initiation by *MacNeice et al.* [2004]. The final breakout CME speeds were always of order the maximum Alfven speed in the system (occurring low in the corona) and increased substantially when the initial field strengths were increased.

[34] A similar comparison was made by *Owens et al.* [2005] between the average radial speed and average magnetic field strength in ICMEs; however, they found no significant correlation between the two quantities for the magnetic cloud subset. There are obvious differences in our event lists, but the discrepancy is most likely explained by the relationship between the LFF model parameter B_0 and the observed average field strength. In low-impact model fits the axial field strength should roughly correspond to the observed average field strength $\langle B \rangle$, but in higher-impact spacecraft trajectories, B_0 should be systematically higher than the observed field magnitudes, up to a factor 2 due to the LFF model's 2:1 axial-to-boundary field strength ratio. To directly compare with the statistics used by *Owens et al.* [2005], we have calculated the Spearman correlation coefficient for our MC list (B_0, $\langle V_r \rangle$), yielding $r_S = 0.21$ with a t-value of 2.44 which indicates significance at the 98.47% level, or a 1.5% chance of no correlation.

3.3. MC Helicity Correlation With $\langle V_r \rangle$

[35] The upper panel of Figure 5 shows the resulting helicity histogram. The dark gray bars represent the entire survey set, whereas the white bars are the fast cloud histogram overplotted. The lower panel shows the calcu-

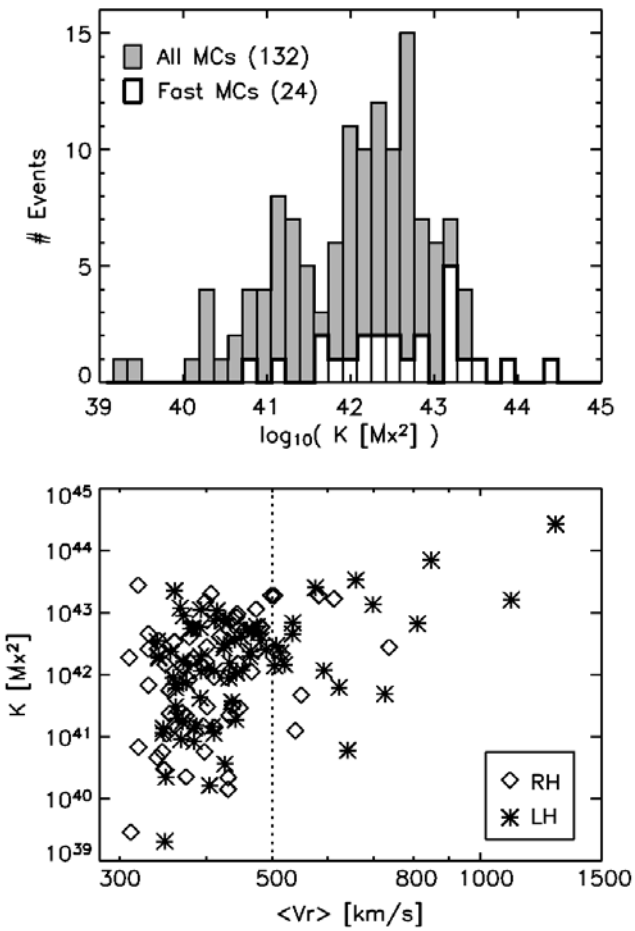

Figure 5. The top panel shows the histogram of MC helicity magnitude in gray bars and the fast event histogram is overplotted in white. The bottom panel shows the distribution of the calculated model helicity and the event averaged radial velocity on a log-log scale. The correlations between R_c, B_0 and $\langle V_r \rangle$ are also manifested in K.

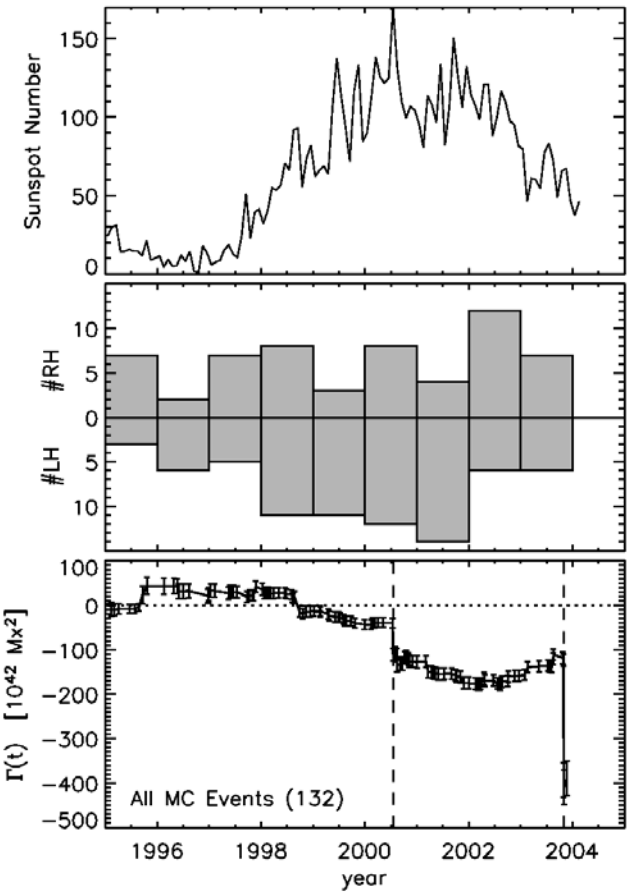

Figure 6. The top panel shows the sunspot number as a proxy for solar activity. The middle panel shows the histogram of total number of right- and left-handed MC events each year. The lower panel plots the net cumulative helicity $\Gamma(t)$, given by equation (5), for all of the magnetic cloud events. The two vertical dashed lines show the largest fast MC events, the Bastille Day 2000 and the 28 October 2003 Halloween event.

lated helicity K for each event plotted against the average radial speed on a log-log scale. The weighted t-statistic with δK^{-1} weights is $|t_w| = 1.86$, corresponding to a 6.2% probability that the K values have no correlation with $\langle V_r \rangle$. For comparison with the *Owens et al.* [2005] method, the Spearman correlation coefficient $r_S = 0.38$ has its t-value = 4.68, indicating a 7.6×10^{-4}% probability of no significant correlation. The vertical dotted line at 500 km/s is the LY03 division between fast and slow magnetic clouds, motivated in a large part by the factor 2–3 difference in the averages of the highest iron charge states. The (K, $\langle V_r \rangle$) distribution shows more of a qualitative difference between the two speed regimes than was apparent in either plot of Figure 4. The Kolmogorov-Smirnov test [*Press et al.*, 1992] indicates that the probability of the observed fast MC helicities being drawn from the observed slow MC helicity distribution function is only 2.5%.

[36] We have shown that estimates of the size, field strength, and consequently flux and helicity of observed magnetic clouds are in some way related to, or at least ordered by, the event speed. As discussed above, CME and ICME velocities are solar cycle–dependent, reflecting the evolution of their sources, namely active regions. In the next section, we will show that for the most common (slow) MCs, the Sun has a preference for shedding flux of a particular handedness during different phases of the activity cycle.

4. MC Helicity Over the Solar Cycle

4.1. Net Cumulative Helicity Evolution

[37] The net helicity gives the running cumulative total of the difference between right-handed (positive) and left-handed (negative) helicity carried by magnetic clouds into the heliosphere. It is defined as the sum of each individual cloud's helicity with the appropriate sign indicating its handedness,

$$\Gamma(t) = \sum_n H_n K_n \delta(t - t_n). \tag{5}$$

Here, K_n, t_n are the helicity (equation (4)) and event time of the nth magnetic cloud and H_n is the flux-rope chirality.

[38] Figure 6 plots this evolution of this MC net helicity over the solar cycle. The top panel shows the sunspot number as a measure of solar activity, the middle panel plots the number of left and right-handed magnetic cloud events per year, and the net helicity is shown in the bottom panel. The estimates of the $\Gamma(t)$ error bars are described in Appendix A.

[39] The most noticeable feature of the net helicity curve is that there are several abrupt steps. The two largest steps, marked with vertical dashed lines, correspond to the Bastille Day 2000 and the fastest Halloween 2003 magnetic cloud events. These events are the largest events in the helicity distribution and they both have left-handed chirality. The helicity of the Bastille Day 2000 cloud is $\sim 7.0 \times 10^{43}$ Mx^2, originating from AR 8270 in the Northern Hemisphere. The Halloween 2003 event was even more impressive, carrying a helicity of $\sim 2.0 \times 10^{44}$ Mx^2, but this LH event was launched from AR 10486 in the Southern Hemisphere, disobeying the hemispheric chirality rule. That being said, AR 10486 was incredibly complex, so it may not be surprising that this particular event did not follow the general helicity association.

[40] Figure 6 clearly shows the underlying structure to the net cumulative helicity evolution over the solar cycle. A left-handed preference develops from about 1997 through 2002 before the curve appears to reverse direction and runs into the Halloween event. The significant discrepancy between the number of LH and RH magnetic clouds from 1997 to 2001 has also been reported by *Huttunen et al.* [2005]. To further examine this trend, we have separated the net helicity curve into the contributions from clouds in our slow and fast velocity categories.

4.2. Slow and Fast MC Net Cumulative Helicity

[41] A vast majority (82%, 108 events) of our magnetic clouds fall into the slow cloud category with $\langle V_r \rangle < 500$ km/s. The fastest clouds, $\langle V_r \rangle \geq 500$ km/s, only make up 18% (24 events) of the survey. We have shown, however, that these events frequently carry the most flux and helicity.

[42] Figure 7 plots the net cumulative helicity for slow and fast magnetic clouds separately, as well as the sunspot

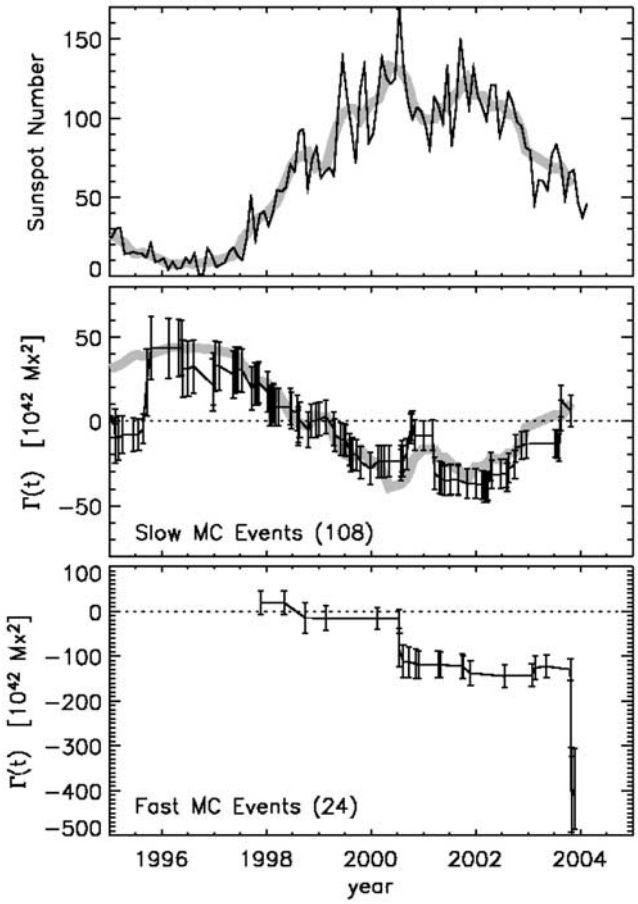

Figure 7. The net helicity solar cycle evolution for magnetic clouds divided into speed categories. The top panel is again sunspot number, with the thick gray line $X \equiv$ the sunspot number smoothed with a 5-month boxcar filter and sampled at the slow MC event times. The middle panel is the net cumulative helicity $\Gamma(t)$ calculated for slow events ($\langle V_r \rangle < 500$ km/s) and a linearly transformed version of the smoothed sunspot number from above to show the qualitative agreement between the main features. The bottom panel is the net cumulative helicity for the fast events ($\langle V_r \rangle \geq 500$ km/s).

number as the solar activity measure. The thick light gray line plotted over the sunspot number is a 5-month boxcar-averaged sunspot number sampled at the slow MC event times. It is immediately apparent in the middle panel that the right- and left-handed helicity preference of the slow clouds is much more ordered by the activity cycle. In fact, the major features of the slow cloud net helicity are qualitatively similar to the large scale features in the sunspot number, such as the rising phase and the double peak. A linear transformation, $X' = -0.662X + 48.75$, of the smoothed, sampled sunspot number X is also plotted over the slow MC net cumulative helicity profile. The two curves overlap almost embarrassingly well.

[43] The slow cloud net helicity maximum and minimum are approximately equal, and while our zero level was an arbitrary starting point, it appears that due to its quasi-sinusoidal nature and the more-or-less even number of right- and left-handed events (51 RH, 57 LH), the the slow cloud net helicity would average to our zero-level over a solar cycle timescale. In other words, equal amounts of right- and left-handed flux and helicity will be shed by normal (slow) magnetic clouds during the solar cycle, as perhaps intuitively expected.

[44] The helicity rate of injection into the corona can be written as two components, an integral of the helicity generated by surface motions and an integral representing helicity emerging through this surface [*Berger*, 1999; *Nindos et al.*, 2003]. Basic observations suggest that the velocities on and through the solar surface are symmetric about the equator and the magnetic field is antisymmetric. This is certainly true for differential rotation acting on a dipolar field. Under these circumstances, both the surface motion and emergence components vanish over the entire solar surface and no net helicity is generated. This implies any local positive helicity in one hemisphere has an equal amount of negative helicity in the other. The question remains, however, whether the corona prefers ejecting helicity of a particular sign. Numerical simulations by *Phillips et al.* [2005] investigating the role of helicity in triggering coronal mass ejections have shown that it is the increase in magnetic free energy rather than the accumulation of local helicity density that is required for an eruption. Therefore the eruption process and subsequent helicity transport into the heliosphere is unlikely to favor a particular chirality. However, our MC observations show that the time it takes the Sun to correct for an excess of flux/helicity of a given handedness seems to be on the order of years.

[45] The same statistical methods can be used to quantify the correlation between the slow MC net helicity and the solar activity curve X. Figure 8 plots the (X, $\Gamma_{\rm slow}$) points in the same style as Figures 4 and 5. The weighted t-statistic with $\delta\Gamma_{\rm slow}^{-1}$ weighting, yields $|t_w| = 6.69$, corresponding to a probability of uncorrelated data of 2.26×10^{-9}%. The Spearman correlation coefficient $r_S = -0.85$ has a t-value magnitude of 31.53, or a 1.36×10^{-28}% chance of no correlation in these data. The net helicity content of the most common (slow) magnetic clouds appears to be modulated by

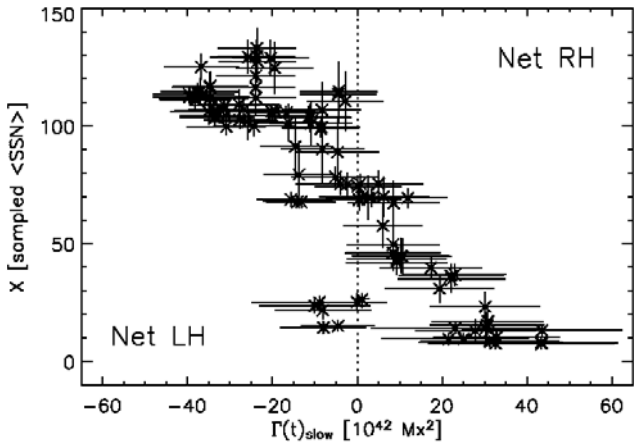

Figure 8. The values of the smoothed, sampled sunspot number X (thick gray line in top panel of Figure 7) plotted versus the slow MC net cumulative helicity. The significant (anti)correlation is apparent and quantified in the text.

the solar activity cycle but the total MC net cumulative helicity is largely due to a small number of the fastest events.

[46] The lower panel of Figure 7 shows that the fast clouds are disproportionately left-handed (71%, 17 events) over the whole data set. During the development of the left-handed preference in the slow cloud net helicity profile (1998–2001), the left-handed fast clouds outnumber right-handed ones 13-2. The fast cloud net helicity is obviously dominated by the two largest events discussed earlier. Besides those two events, there is a slight indication that the fast cloud net helicity appears to show the same general property as the slow clouds with about a year phase shift. There are four RH fast MCs in just the 2003 data. It will be interesting to see if this is an indication of trend reversal and there is an overabundance of large, right-handed MCs either later in the declining phase or during the next cycle to offset the observed left-handed helicity bias thus far.

5. Discussion

[47] We have clearly shown there is an ordering of magnetic cloud ICMEs beyond their occurrence rates associated with the solar activity cycle. This ordering manifests itself in the net helicity which measures the cumulative difference between the amount of right- and left-handed helicity transported into the heliosphere. We have divided our magnetic clouds by their average radial velocity into two categories and shown that the fast events, and primarily a few ''super'' events, like the Bastille Day 2000 and Halloween 2003 magnetic clouds, dominate the helicity totals. The net helicity profile of normal (slow) MCs appear to track the solar activity cycle. We also note that the superposition of these CMEs with one dominant helicity will have important consequences for cosmic ray transport, as discussed by *Bieber et al.* [1987b].

[48] The net helicity profiles of these highly structured ICMEs lead us to conclude that the physical mechanisms that generate CME helicity cannot be exclusively symmetric about the equator. A helicity generating mechanism that was symmetric about the equator, either differential rotation at the surface or some interior process, will produce equal and opposite amounts of helicity in the two solar hemispheres. We have just shown that the solar cycle appears to modulate the chirality and helicity of at least the most common (slow) magnetic cloud ICMEs, indicating that some significant fraction of the MC helicity content has to be from a time-varying source. We may be measuring the heliospheric manifestation of observable long-term asymmetries in the size, shear, or complexity of active regions, although, to the best of our knowledge, no dynamo model explicitly predicts hemispheric or chirality asymmetry in new cycle field generation.

[49] There are a number of solar activity indices that show long-term asymmetries that appear to be consistent with our results. For example, *Vernova et al.* [2002] calculate a ''vector'' sunspot area and finds a persistent average pattern of Northern Hemisphere dominance that transitions to Southern Hemisphere dominance right before the solar pole reversal. More recently, *Kane* [2005] looked at the solar flare index during cycles 21 and 22 and also finds a multiyear northern preference that transitions to a multiyear southern preference around or after the polarity reversal at solar maximum. Our slow MC cumulative helicity profile matches the trend of both the *Vernova et al.* [2002] and *Kane* [2005] results assuming the general correspondence of the hemispheric helicity rule (N↔LH, S↔RH) but appears more in-phase with the *Kane* solar flare index.

[50] The other interesting conjecture from our results is about the infrequent super events, such as the Bastille Day 2000 and the Halloween 2003 MCs. Whereas most MC events appear to contain a mixture of active region (sheared) and overlying (potential) coronal fields [*Leamon et al.*, 2004], the fluxes and helicity of these fastest/largest events are approximately an order of magnitude above the mean and define the upper limit of our flux and helicity distributions. Numerical simulations of the breakout model for CME initiation show that a significant portion of the injected helicity can remain in the corona after the eruption [*MacNeice et al.*, 2004; *Phillips et al.*, 2005]. However, the magnetic topology in these idealized simulations is global scale, i.e., the null point is high in the corona and the overlying, restraining field is relatively weak. In the active region sources for the Bastille Day 2000 and Halloween 2003 events, the complex magnetic topology produced multipolar flux systems (favorable for a breakout eruption scenario) that were entirely contained in the strong field active regions [*Aulanier et al.*, 2000; I. I. Roussev, private communication, 2005]. We speculate that these super MC events must be primarily composed of the strongest active region fields, and their solar eruptions must have opened up very low-lying active region flux.

Appendix A: Flux and Net Helicity Error Analysis

[51] To estimate the uncertainty of the helicity K of each event, we must include a measure of the uncertainties in all of the linear force-free fit parameters ϕ_0, θ_0, ρ_0, and B_0, as well as the uncertainty in the cloud duration, ΔT, and the average radial velocity $\langle V_r \rangle$.

[52] From equation (4) we see $K \propto B_0^2 R_c^3$. The fractional uncertainties for the fluxes and helicity as functions of the linear force-free cylinder fit parameters are

$$\frac{\delta\Phi_t}{\Phi_t} = \sqrt{\left(\frac{\delta B_0}{B_0}\right)^2 + \left(2\frac{\delta R_c}{R_c}\right)^2}, \tag{A1}$$

$$\frac{\delta\Phi_p}{\Phi_p} = \sqrt{\left(\frac{\delta B_0}{B_0}\right)^2 + \left(\frac{\delta R_c}{R_c}\right)^2}, \tag{A2}$$

$$\frac{\delta K}{K} = \sqrt{\left(2\frac{\delta B_0}{B_0}\right)^2 + \left(3\frac{\delta R_c}{R_c}\right)^2}, \tag{A3}$$

assuming B_0 and R_c are independent quantities. While we have shown in section 3 that there is a definite physical correlation in the data between events with strong field and a large model cylinder radius (in their correlation with $\langle V_r \rangle$), they are independent quantities with respect to the model fitting. The cloud radius R_c is a function of the fit

parameters ϕ_0, θ_0, ρ_0, the cloud duration, and the average radial velocity. LY03 showed that there was no significant correlation between B_0 and ρ_0, ϕ_0, or θ_0 during the error minimization used to determine the "best-fit" parameters.

[53] The cloud radius R_c is calculated as,

$$R_c(\phi_0, \theta_0, \rho_0, \Delta T, \langle V_r \rangle) = \frac{\Delta T \langle V_r \rangle}{2\sqrt{1-\rho_0^2}} \sqrt{\sin^2\theta_0 + \cos^2\theta_0 \sin^2\phi_0}, \tag{A4}$$

which is identical to equation (17) of *Lepping et al.* [2003] except for the notation differences ($\rho_0 \equiv Y_0/R_c$, etc.).

[54] Equation (A4) can be used to derive the expression for the cloud radius uncertainty,

$$\delta R_c^2 = \left(\frac{\partial R_c}{\partial \phi_0}\delta\phi_0\right)^2 + \left(\frac{\partial R_c}{\partial \theta_0}\delta\theta_0\right)^2 + \left(\frac{\partial R_c}{\partial \rho_0}\delta\rho_0\right)^2 + \left(\frac{\partial R_c}{\partial \Delta T}\delta\Delta T\right)^2 + \left(\frac{\partial R_c}{\partial \langle V_r\rangle}\delta\langle V_r\rangle\right)^2. \tag{A5}$$

Equation (A5) again assumes all these variables are independent, which is not the case. The fit parameters ϕ_0, θ_0, and ρ_0 can be highly correlated in individual events [LY03]. However, since (A5) will tend to overestimate the actual uncertainty, we will use it as an estimate of the upper limit. We also constrain each of the individual parameter fractional uncertainties to 1.0 because certain values of the fit parameters misbehave, i.e., yield poor or unphysical fits, $\rho_0 \geq \sim 0.7$, or both θ_0, $\phi_0 \approx 0$.

[55] The values for the uncertainties for each fit parameter are estimated from the MPFIT fitting routine covariance matrices (http://cow.physics.wisc.edu/~craigm/idl/fitting.html) and averaged over all events. This yields,

$$\langle \delta\phi_0 \rangle = 37 \pm 26^\circ, \tag{A6}$$

$$\langle \delta\theta_0 \rangle = 22 \pm 15^\circ, \tag{A7}$$

$$\langle \delta\rho_0 \rangle = 0.24 \pm 0.26, \tag{A8}$$

and we assume $\delta B_0 = 0.10\ B_0$, all of which agree well with the findings of other researchers [*Lepping et al.*, 2003]. The uncertainties for the data parameters are taken as

$$\delta\Delta T = 2 \text{ hours}, \tag{A9}$$

$$\delta\langle V_r \rangle = \text{stddev}[V_r]. \tag{A10}$$

[56] Equation (5) defines the net cumulative helicity Γ. Now we can write the error bars for each element Γ_n, the nth measurement in the estimate of the net cumulative helicity. This is simply the quadratic sum of the helicity uncertainties for every event, divided by the number of measurements (MC events) used in the estimate,

$$\frac{\delta\Gamma_n}{\Gamma_n} = \sqrt{\frac{1}{n}\sum_{j=1}^{n}\left(\frac{\delta K_j}{K_j}\right)^2}. \tag{A11}$$

[57] **Acknowledgments.** The authors thank Andrew C. Mawikere for his valuable contribution as part of the 2002–2003 Undergraduate Research Opportunity program at the University of Michigan. This work is supported by ONR and NASA. BJL is supported by a NASA GSRP fellowship NGT5-50453. The authors also thank the ACE MAG and SWEPAM teams for their level 2 data available on the ACE Science Center Web site http://www.srl.caltech.edu/ACE/ASC/ as well as the Wind MFI and SWE teams for making their data available at http://www-lep.gsfc.nasa.gov/mfi/windmfi.html and http://web.mit.edu/space/www/wind/wind_data.html, respectively.

[58] Shadia Rifai Habbal thanks Richard C. Canfield and Robert J. Leamon for their assistance in evaluating this paper.

References

Andrews, M. D. (2002), Characteristics of CMEs associated with big flares, in *Solar Variability: From Core to Outer Frontiers, Proceedings of 10th European Solar Physics Meeting*, *ESA SP-506*, pp. 531–534, Eur. Space Agency, Prauge, Czech Republic.

Aulanier, G., E. E. DeLuca, S. K. Antiochos, R. A. McMullen, and L. Golub (2000), The topology and evolution of the Bastille day flare, *Astrophys. J.*, *540*, 1126.

Berger, M. A. (1999), Magnetic helicity in space physics, in *Magnetic Helicity in Space and Laboratory Plasmas*, *Geophys. Monogr. Ser.*, vol. 111, edited by M. R. Brown, R. C. Canfield, and A. A. Pevtsov, pp. 1–9, AGU, Washington, DC.

Berger, M. A., and A. Ruzmaikin (2000), Rate of helicity production by solar rotation, *J. Geophys. Res.*, *105*(A5), 10,481.

Bieber, J. W., and D. M. Rust (1995), The escape of magnetic flux from the sun, *Astrophys. J.*, *453*, 911.

Bieber, J. W., P. A. Evenson, and W. H. Matthaeus (1987a), Magnetic helicity of the Parker field, *Astrophys. J.*, *315*, 700.

Bieber, J. W., P. A. Evenson, and W. H. Matthaeus (1987b), Magnetic helicity of the IMF and the solar modulation of cosmic rays, *Geophys. Res. Lett.*, *14*(8), 864.

Bothmer, V., and D. M. Rust (1997), The field configuration of magnetic clouds and the solar cycle, in *Coronal Mass Ejections*, *Geophys. Monogr. Ser.*, vol. 99, edited by N. Crooker, J. Joselyn, and J. Feynman, pp. 139–146, AGU, Washington, DC.

Bothmer, V., and R. Schwenn (1998), The structure and origin of magnetic clouds in the solar wind, *Ann. Geophys.*, *16*, 1.

Brown, M. R., R. C. Canfield, and A. A. Pevtsov (Eds.) (1999), *Magnetic Helicity in Space and Laboratory Plasmas*, *Geophys. Monogr. Ser.*, vol. 111, AGU, Washington, DC.

Brueckner, G. E., et al. (1995), The Large Angle Spectroscopic Coronagraph (LASCO), *Solar Phys.*, *162*, 357.

Burlaga, L. F. (1988), Magnetic clouds and force-free fields with constant alpha, *J. Geophys. Res.*, *93*(A7), 7217.

Burlaga, L. F. (1991), Magnetic clouds, in *Physics of the Inner Heliosphere*, vol. II, edited by R. Schwenn and E. Marsch, pp. 1–21, Springer, New York.

Cane, H. V., and I. G. Richardson (2003), Interplanetary coronal mass ejections in the near-Earth solar wind during 1996–2002, *J. Geophys. Res.*, *108*(A4), 1156, doi:10.1029/2002JA009817.

Canfield, R. C., and A. A. Pevtsov (1999), Helicity and reconnection in the solar corona: Observations, in *Magnetic Helicity in Space and Laboratory Plasmas*, *Geophys. Monogr. Ser.*, vol. 111, edited by M. R. Brown, R. C. Canfield, and A. A. Pevtsov, pp. 197–204, AGU, Washington, DC.

Crooker, N. U., J. T. Gosling, and S. W. Kahler (2002), Reducing heliospheric magnetic flux from coronal mass ejections without disconnection, *J. Geophys. Res.*, *107*(A2), 1028, doi:10.1029/2001JA000236.

Dasso, S., C. H. Mandrini, P. Démoulin, and C. J. Farrugia (2003), Magnetic helicity analysis of an interplanetary twisted flux tube, *J. Geophys. Res.*, *108*(A10), 1362, doi:10.1029/2003JA009942.

Démoulin, P., C. H. Mandrini, L. van Driel-Gesztelyi, B. J. Thompson, S. Plunkett, Z. s. Kővári, G. Aulanier, and A. Young (2002), What is the source of the magnetic helicity shed by CMEs? The long-term helicity budget of AR 7978, *Astron. Astrophys.*, *382*, 650 doi:10.1051/0004-6361:20011634.

DeVore, C. R. (2000), Magnetic helicity generation by solar differential rotation, *Astrophys. J.*, *539*, 944.

Ding, Y. J., Q. F. Hong, and H. Z. Wang (1987), A statistical study of the spiral spots on the solar disc, *Solar Phys.*, *107*, 221.

Gopalswamy, N., A. Lara, S. Yashiro, and R. A. Howard (2003a), Coronal mass ejections and solar polarity reversal, *Astrophys. J.*, *598*, L63.

Gopalswamy, N., A. Lara, S. Yashiro, S. Nunes, and R. A. Howard (2003b), Coronal mass ejection activity during solar cycle 23, *Solar Variability as an Input to the Earth's Environment*, edited by A. Wilson, pp. 403–414, ESA Publ., Tatranská Lomnica, Slovakia.

Green, L. M., M. C. López-Fuentes, C. H. Mandrini, P. Dmoulin, L. Van Driel-Gesztelyi, and J. L. Culhane (2002), The magnetic helicity budget of a CME-prolific active region, *Solar Phys.*, *208*, 43.

Huttunen, K. E. J., R. Schwenn, V. Bothmer, and H. E. J. Koskinen (2005), Properties and geoeffectiveness of magnetic clouds in the rising, maximum and early declining phases of solar cycle 23, *Ann. Geophys.*, *23*, 625.

Kane, R. P. (2005), North-south asymmetry of some solar indices, *J. Atmos. Sol. Terr. Phys.*, *67*(5), 429, doi:10.1016/j.jastp.2004.09.003.

Larson, D. E., et al. (1997), Tracing the topology of the October 18–20, 1995, magnetic cloud with $\sim 0.1-10^2$ keV electrons, *Geophys. Res. Lett.*, *24*, 15, 1911.

Leamon, R. J., R. C. Canfield, and A. A. Pevtsov (2002), Properties of magnetic clouds and geomagnetic storms associated with eruption of coronal sigmoids, *J. Geophys. Res.*, *107*(A9), 1234, doi:10.1029/2001JA000313.

Leamon, R. J., R. C. Canfield, S. L. Jones, K. Lambkin, B. J. Lundberg, and A. A. Pevtsov (2004), Helicity of magnetic clouds and their associated active regions, *J. Geophys. Res.*, *109*, A05106, doi:10.1029/2003JA010324.

Lepping, R. P., J. A. Jones, and L. F. Burlaga (1990), Magnetic field structure of interplanetary magnetic clouds at 1 AU, *J. Geophys. Res.*, *95*(A8), 11,957.

Lepping, R. P., et al. (2001), The Bastille Day magnetic clouds and upstream shocks: Near-Earth interplanetary observations, *Solar Phys.*, *204*, 287.

Lepping, R. P., D. B. Berdichevsky, and T. J. Ferguson (2003), Estimated errors in magnetic cloud model fit parameters with force-free cylindrically symmetric assumptions, *J. Geophys. Res.*, *108*(A10), 1356, doi:10.1029/2002JA009657.

Low, B. C. (1996), Solar activity and the corona, *Solar Phys.*, *167*, 217.

Low, B. C. (1997), The role of coronal mass ejections in solar activity, in *Coronal Mass Ejections*, *Geophys. Monogr. Ser.*, vol. 99, edited by N. Crooker, J. Joselyn, and J. Feynman, pp. 147–156, AGU, Washington, DC.

Low, B. C. (2001), Coronal mass ejections, magnetic flux ropes, and solar magnetism, *J. Geophys. Res.*, *106*(A11), 25,141.

Lundquist, S. (1950), Magnetohydrostatic fields, *Ark. Fys.*, *2*, 361.

Lynch, B. J., T. H. Zurbuchen, L. A. Fisk, and S. K. Antiochos (2003), Internal structure of magnetic clouds: Plasma and composition, *J. Geophys. Res.*, *108*(A6), 1239, doi:10.1029/2002JA009591.

MacNeice, P. J., S. K. Antiochos, A. Phillips, D. S. Spicer, C. R. DeVore, and K. Olson (2004), A numerical study of the breakout model for CME initiation, *Astrophys. J.*, *614*, 1028, doi:10.1086/423887.

MacQueen, R. M., and R. R. Fisher (1983), The kinematics of solar inner coronal transients, *Solar Phys.*, *89*, 89.

Martin, S. F., and A. H. McAllister (1996), The skew of X-ray coronal loops overlying Hα filaments, in *Magnetohydrodynamic Phenomona in the Solar Atmosphere, Prototypes of Stellar Magnetic Activity*, edited by Y. Uchida, H. S. Hudson, and T. Kosugi, pp. 497–498, Springer, New York.

Martin, S. F., R. Bilimoria, and P. W. Tracadas (1994), Magnetic field configurations basic to filament channels and filaments, in *Solar Surface Magnetism*, *NATO ASI Ser. C*, vol. 433, edited by R. J. Rutten and C. J. Schrijver, pp. 303–338, Springer, New York.

Marubashi, K. (1997), Interplanetary magnetic flux ropes and solar filaments, in *Coronal Mass Ejections*, *Geophys. Monogr. Ser.*, vol. 99, edited by N. Crooker, J. Joselyn, and J. Feynman, pp. 147–156, AGU, Washington, DC.

Matthaeus, W. H., and M. L. Goldstein (1982), Measurement of the rugged invariants of magnetohydrodynamic turbulence in the solar wind, *J. Geophys. Res.*, *87*(A8), 6011.

McComas, D. J., J. T. Gosling, C. M. Hammond, M. B. Moldwin, J. L. Phillips, and R. J. Forsyth (1995), Reconnection on open field lines ahead of coronal mass ejections, *Space Sci. Rev.*, *72*, 129.

Nindos, A., and H. Zhang (2002), Photospheric motions and coronal mass ejection productivity, *Astrophys. J.*, *573*, L133.

Nindos, A., J. Zhang, and H. Zhang (2003), The magnetic helicity budget of solar active regions and coronal mass ejections, *Astrophys. J.*, *594*, 1033.

Owens, M. J., P. J. Cargill, C. Pagel, G. L. Siscoe, and N. U. Crooker (2005), Characteristic magnetic field and speed properties of interplanetary coronal mass ejections and their sheath regions, *J. Geophys. Res.*, *110*, A01105, doi:10.1029/2004JA010814.

Parker, E. N. (1963), *Interplanetary Dynamical Processes*, Interscience, New York.

Pevtsov, A. A., and R. C. Canfield (1999), Helicity of the photospheric magnetic field, in *Magnetic Helicity in Space and Laboratory Plasmas*, *Geophys. Monogr. Ser.*, vol. 111, edited by M. R. Brown, R. C. Canfield, and A. A. Pevtsov, pp. 197–204, AGU, Washington, DC.

Pevtsov, A. A., R. C. Canfield, and T. R. Metcalf (1995), Latitudinal variation of helicity of photospheric magnetic fields, *Astrophys. J.*, *440*, L109.

Pevtsov, A. A., R. C. Canfield, and S. M. Latushko (2001), Hemispheric helicity trend for solar cycle 23, *Astrophys. J.*, *549*, L263.

Phillips, A. D., P. J. MacNeice, and S. K. Antiochos (2005), The role of magnetic helicity in coronal mass ejections, *Astrophys. J.*, *624*, L129.

Porter, L. J., and J. A. Klimchuk (1995), Soft X-ray loops and coronal heating, *Astrophys. J.*, *454*, 499.

Press, W. H., S. A. Teukolsky, W. T. Vetterling, and B. P. Flannery (1992), *Numerical Recipes in Fortran 77: The Art of Scientific Computing*, 2nd ed., Cambridge Univ. Press, New York.

Rees, A., and R. J. Forsyth (2003), Magnetic clouds with east/west oriented axes observed by Ulysses during solar cycle 23, *Geophys. Res. Lett.*, *30*(19), 8030, doi:10.1029/2003GL017296.

Reinard, A. A., and L. A. Fisk (2004), Reconnection of magnetic field lines near the solar surface during coronal mass ejection propagation, *Astrophys. J.*, *608*, 533.

Richardson, I. G., and H. V. Cane (1995), Regions of abnormally low proton temperature in the solar wind (1965–1991) and their association with ejecta, *J. Geophys. Res.*, *100*(A12), 23,397.

Richardson, R. S. (1941), The nature of solar hydrogen vortices, *Astrophys. J.*, *93*, 24.

Riley, P., and N. U. Crooker (2004), Kinematic treatment of coronal mass ejection evolution in the solar wind, *Astrophys. J.*, *600*, 1035.

Riley, P., J. A. Linker, R. Lionello, Z. Mikic, D. Odstrcil, M. A. Hidalgo, Q. Hu, R. P. Lepping, B. J. Lynch, and A. Rees (1994), Fitting flux ropes to a global MHD solution: A comparison of techniques, *J. Atmos. Sol. Terr. Phys.*, *66*, 15–16, 1321, doi:10.1016/j.jastp.2004.03.019.

Rust, D. M. (1994), Spawning and shedding of helical field in the solar atmosphere, *Geophys. Res. Lett.*, *21*, 241.

Rust, D. M. (1997), Helicity conservation, in *Coronal Mass Ejections*, *Geophys. Monogr. Ser.*, vol. 99, edited by N. Crooker, J. Joselyn, and J. Feynman, pp. 119–125, AGU, Washington, DC.

Rust, D. M. (2001), A new paradigm for solar filament eruptions, *J. Geophys. Res.*, *106*(A11), 25,075.

Sheeley, N. R., Jr., R. A. Howard, M. J. Koomen, D. J. Michels, R. Schwenn, K. H. Mühlhäuser, and H. Rosenbauer (1985), Coronal mass ejections and interplanetary shocks, *J. Geophys. Res.*, *90*(A1), 163.

Shodhan, S., N. U. Crooker, S. W. Kahler, R. J. Fitzenreiter, D. E. Larson, R. P. Lepping, G. L. Siscoe, and J. T. Gosling (2000), Counterstreaming electrons in magnetic clouds, *J. Geophys. Res.*, *105*(A12), 27,261.

Smith, C. W. (1999), Solar-cyle, radial and latitudinal variations of magnetic helicity: IMF observations, in *Magnetic Helicity in Space and Laboratory Plasmas*, *Geophys. Monogr. Ser.*, vol. 111, edited by M. R. Brown, R. C. Canfield, and A. A. Pevtsov, pp. 239–245, AGU, Washington, DC.

Vernova, E. S., K. Mursula, M. I. Tyasto, and D. G. Baranov (2002), A new pattern for the north-south asymmetry of sunspots, *Solar Phys.*, *205*, 371.

Yurchyshyn, V. B., H. Wang, P. R. Goode, and Y. Deng (2001), Orientation of the magnetic field in interplanetary flux ropes and solar filaments, *Astrophys. J.*, *563*, 381.

Zhang, J., M. W. Liemohn, J. U. Kozyra, B. J. Lynch, and T. H. Zurbuchen (2004), A statistical study of the geoeffectiveness of magnetic clouds during high solar-activity years, *J. Geophys. Res.*, *109*, A09101, doi:10.1029/2004JA010410.

Zhang, M., and B. C. Low (2001), Magnetic flux emergence into the solar corona I: Its role for the reversal of global coronal magnetic fields, *Astrophys. J.*, *561*, 406.

S. K. Antiochos, E. O. Hulburt Center for Space Research, Naval Research Laboratory, Washington, DC 20375, USA.

J. R. Gruesbeck, B. J. Lynch, and T. H. Zurbuchen, Department of Atmospheric, Oceanic, and Space Sciences, University of Michigan, 2455 Hayward St., Ann Arbor, MI 48109, USA. (lynchb@engin.umich.edu)